Reaffirmation of probe dependence of the mass deformation length for low-lying excitations in ^{112,116,118,120,122,124}Sn isotopes

A. Kundu,[1,2,*] S. Santra,[1,2] A. Pal,[1,2] D. Chattopadhyay,[1,2,†] T. N. Nag,[2,3] R. Gandhi,[1] P. C. Rout,[1,2] B. J. Roy,[1,2] B. K. Nayak,[1,2] and S. Kailas[1,4]

[1]*Nuclear Physics Division, Bhabha Atomic Research Centre, Mumbai 400085, India*
[2]*Homi Bhabha National Institute, Anushakti Nagar, Mumbai 400094, India*
[3]*Radiochemistry Division, Bhabha Atomic Research Centre, Mumbai 400085, India*
[4]*Manipal Center for Natural Sciences, Manipal Academy of Higher Education, Manipal 576104, India*

(Received 6 May 2019; revised manuscript received 17 July 2019; published 13 August 2019)

Background: A transparent approach for the study of nuclear shapes and sizes in excited states requires knowledge about dynamic deformations of both neutron and proton distributions, by means of their independent excitations at the same energy. Heavy-ion scattering could be a reliable approach, facilitating a simultaneous study of deformations of charge and matter densities in nuclei.
Purpose: Measurement of angular distributions of the inelastic scattering cross sections for excitations to low-lying 2_1^+ and 3_1^- states in ^{112,116,118,120,122,124}Sn nuclei using ^{12}C beam as a probe at $E_{\rm lab} = 60$ MeV, and determination of neutron and proton transition matrix elements involved in each excitation.
Methods: Projectilelike fragments have been detected using ten sets of Si-surface barrier detector telescopes to measure the cross sections for elastic and inelastic scattering channels. Coupled reaction channels calculations are performed to understand the measured differential cross sections.
Results: Homogeneous nature of surface vibrations (similar deformation for proton and neutron distributions) for the 2_1^+ and 3_1^- states in Sn isotopes is observed.
Conclusions: A comparison with recent results using ^{7}Li projectile at similar $E_{\rm c.m.}/V_{\rm B}$, which showed damped neutron vibrations particularly for the 3_1^- state, confirms that such measurements are probe dependent. Intrinsic transition matrix elements of nuclei can be deduced by removing the effects of finite projectile size in the extraction of nuclear shapes.

DOI: 10.1103/PhysRevC.100.024614

I. INTRODUCTION

The determination of nuclear shapes in their excited states is one of the traditional problems of nuclear physics. From electromagnetic measurements, a large volume of information is present about the distribution of charge (primarily, protons) in nuclei. Estimates of the neutron distribution are largely dependent on the choice of nuclear interactions. In some systems, the excitation spectrum is better described within a collective model: a homogeneous neutron-proton fluid undergoing shape oscillations about the equilibrium, with their respective transition densities in the ratio of N/Z. The ratio of the neutron and proton transition matrix elements, M_n/M_p, has commonly been used to identify any inhomogeneity between their transition strengths, in comparison with the collective model value of $M_n/M_p \sim N/Z$. Since M_p can be accessed through electromagnetic measurements, isospin conservation is a convenient approach to deduce M_n, with $M_n(N,Z) = M_p(Z,N)$ [1]. However, this is predominantly applicable for light nuclei and their mirrors. For neutron-excess heavier nuclei, the question of the relative participation of neutron and proton densities in low-lying collective modes is of considerable interest, and heavy-ion collisions offer a reliable substitute for such investigations. Inelastic excitations triggered by heavy-ion collisions occur under the combined influence of electromagnetic and nuclear potentials, and allow a simultaneous investigation of dynamic deformations of both neutron and proton distributions that is not affected by normalization uncertainties. The present work focuses on the extraction and interpretation of nuclear size and shape information from the study of heavy-ion inelastic scattering. The dominant feature, which provides the key to understand such scattering phenomena, is the strong surface absorption of heavy ions; most of the elastically or inelastically scattered projectiles are predominantly involved in a peripheral interaction. The differential inelastic scattering cross sections observed at energies above the Coulomb barrier are commonly found to exhibit distinct patterns, on account of Coulomb-nuclear interference (CNI), which are qualitatively well represented in terms of theoretical models corresponding to strongly absorbed probes.

In addition to the Coulomb potential between nuclei, it has been customary to describe scattering phenomena in terms of an optical potential $V_N(r)$ whose shape is of the same general

*ananyak.delhi@gmail.com
†Present address: Saha Institute of Nuclear Physics, 1/AF, Bidhannagar, Kolkata 700064, India.

form as that of the nuclear density distribution. For nuclei with spherical ground state, the low-lying excited states are pictured as surface vibrations about the mean spherical shape. It is natural to assume that the corresponding potential would follow the deformed shape of the density distribution. This can be expressed as a change in the radius at which the potential is evaluated, the change depending on the relative orientations of the radius vector to the intrinsic orientation of the nucleus. For an axially symmetric deformation in a nucleus, an adequate parametrization of the radius, $R(\theta) = R_0[1 + \sum_\lambda \beta_{\lambda 0} Y^*_{\lambda 0}(\theta)]$, where λ is the multipolarity of the transition, defines $\delta_\lambda = \beta_{\lambda 0} R_0$ as the intrinsic deformation length. In an inelastic scattering event, the deformed charge (proton) and mass (neutron + proton) densities can be approximated by this expansion, with respective radii R_{ch} and R_m. Such a shape parametrization is often a starting point for theoretical calculations, where, the deformed potential can be expressed in terms of both Coulomb and nuclear form factors [2] as,

$$V_\lambda(r) = \sum_\lambda \left[f^C_\lambda(r) + f^N_\lambda(r)\right] Y^*_{\lambda 0}(\hat{r}) \tag{1}$$

with $f^C_\lambda(r) = \delta^{ch}_\lambda [\frac{3 Z_P Z_T e^2 R^{\lambda-1}_{ch}}{(2\lambda+1)\, r^{\lambda+1}}]$, and $f^N_\lambda(r) = -\delta^m_\lambda \frac{dV_N(r)}{dr}$. The transition parameters, δ^{ch}_λ and δ^m_λ, are referred to as the charge and mass (or, potential) deformation lengths, respectively. These quantities are sensitive to deviations in charge and mass distributions from equilibrium shapes. The shape of the differential cross section across a wide angular range allows a simultaneous determination of δ^{ch}_λ and δ^m_λ, from which one extracts a ratio of M_n/M_p uniquely. A discrepancy often exists between the nuclear and Coulomb experimental results. A longstanding difficulty in the comparison has been due to the different radii that characterize the two types of interactions. The mechanism of Coulomb excitation is well understood and the charge radius has been accurately measured by electron scattering to be about $1.2A^{1/3}$fm for a suitably diffuse radial charge distribution. On the contrary, the optical potential radius characterizing the matter distribution may vary from $1.25A^{1/3}$ for collisions with tightly bound probes, to $1.55A^{1/3}$ fm with weakly bound probes, where A is the atomic mass of the target nucleus. Since the extracted nuclear shapes rely on the interaction potential $V_N(r)$ between the nucleus and the probe, it is not surprising that these quantities extracted from scattering of different projectiles are systematically different and indicate discrepant transition rates. A scaling relation proposed by Blair [3], $\delta^m_\lambda \equiv \delta^{\rm pot}_\lambda = \beta_{\lambda 0} R_0$, is widely used to relate the probe-dependent deformation to the true deformation of the nucleus. However, this prescription does not remove all discrepancies that arise due to the nature of the nucleus-nucleus interaction as well as the finite probe size.

The characteristics of the dominant low-lying quadrupole ($0^+_{g.s} \rightarrow 2^+_1; \lambda = 2$) and octupole ($0^+_{g.s} \rightarrow 3^-_1; \lambda = 3$) transitions in Sn isotopes have been extensively studied with a variety of probes like Coulomb excitation, electron, proton, and α scattering. The $\lambda = 2$ electromagnetic transition probabilities, $B(E2)$ [4–8], are often measured with smaller uncertainties. However, the $\lambda = 3$ transition probabilities, $B(E3)$, have a wide range with larger uncertainties [9–15]. In a recent work [16], significant differences between the $\lambda = 3$ charge and mass deformation lengths were observed in all the Sn isotopes under study, using ^{7}Li as the projectile at $E_{\rm c.m.}/V_{\rm B} \approx 1.3$. Lower values of $M_n/M_p(<N/Z)$ were extracted, which led to the conjecture that the $\lambda = 3$ vibration may be inhomogeneous, when excited by ^{7}Li. However, the excitation of the 2^+_1 state was observed to be homogeneous. The target mass deformation lengths, $\delta^m_{2,3}$, were found to be dependent on the choice of the projectile. The main objective of this study is to utilize CNI effects for quantitative assessments of δ^{ch}_λ and δ^m_λ, and deduce the M_n/M_p ratios for the 2^+_1 and 3^-_1 levels in ^{112,116,118,120,122,124}Sn nuclei using the ^{12}C nucleus as probe at similar $E_{\rm c.m.}/V_{\rm B} \approx 1.3$ ($E_{\rm lab} = 60$ MeV; $V_{\rm B} \approx 42$ MeV). Intermediate energy scattering using an isoscalar probe such as ^{12}C can be a useful spectroscopic tool for exciting discrete collective states as such nuclei are sensitive to nuclear matter distributions and the projectile-target interaction is devoid of any spin and isospin dependence. Such probes are complementary to those with unpaired proton(s) or neutron(s). A simultaneous description of differential cross sections for elastic and inelastic scattering channels has been attempted by means of explicit coupled reaction channels (CRC) calculations. A large set of information on probe dependence of target deformation lengths can be reliably used to make an estimate about the intrinsic deformation lengths in nuclei.

The paper is organized as follows. The experimental setup and the data analysis procedure are described in Sec. II. The model calculations using FRESCO [2] that explain the experimental data are described in Sec. III. The method used to arrive at the neutron and proton transition matrix elements is highlighted in Sec. IV, with an estimate of the intrinsic deformation lengths reported in Sec. V. The results are discussed and summarized in Sec. VI.

II. MEASUREMENT AND DATA ANALYSIS

The measurements for angular distributions of elastic and inelastic scattering cross sections have been carried out at the BARC-TIFR Pelletron accelerator facility, Mumbai. Self-supporting enriched (>95%) targets of ^{112,116,118,120,122,124}Sn of thicknesses $\approx$540 μg/cm^2, 1.45 mg/cm^2, 320 μg/cm^2, 280 μg/cm^2, 85 μg/cm^2, and 290 μg/cm^2, respectively, have been used. Ten telescopes (ΔE-E) of Si surface barrier detectors, evenly distributed on two arms of a scattering chamber, each placed 10° apart from its neighboring telescope at a distance of $\approx$21 cm from the target center, are used to detect projectilelike fragments in the angular range of 20°$-$110°. Two other Si surface barrier detectors, mounted at $\pm$20° with respect to the beam at a distance of $\approx$72 cm from the center, are used for beam flux normalization. The detector thicknesses are $\approx$15$-$25 μm for ΔE and $\approx$300$-$1000 μm for the E detectors. A schematic diagram of the setup is shown in Fig. 1.

A typical gain-matched spectrum of ΔE versus $E_{\rm total}(=E + \Delta E)$ is shown for the ^{12}C + ^{112}Sn system in Fig. 2(a), where projectilelike fragments with different Z(=2–7) and A(=4–14) are identified. Typical energy resolution of a telescope is in the range $\approx$75–100 keV ($\approx$170–200 keV for the thicker foil of ^{116}Sn), sufficient to

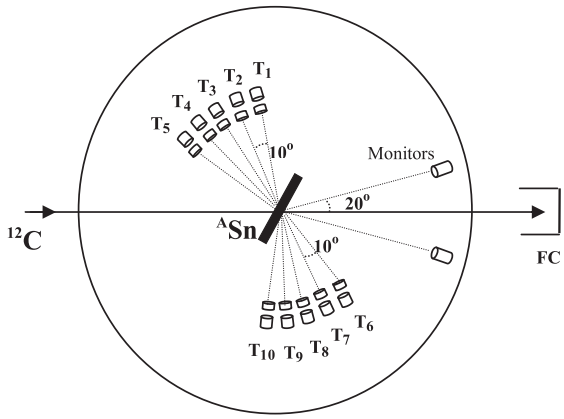

FIG. 1. Schematic diagram of the experimental setup.

resolve the different excited states of interest. Along with the elastic scattered peak, the yields of projectile and target excited states corresponding to the 2_1^+ and 3_1^- vibrational states of ^{112,116,118,120,122,124}Sn as well as the first excited state of ^{12}C (4.438 MeV), are found to be dominant [see Fig. 2(b)].

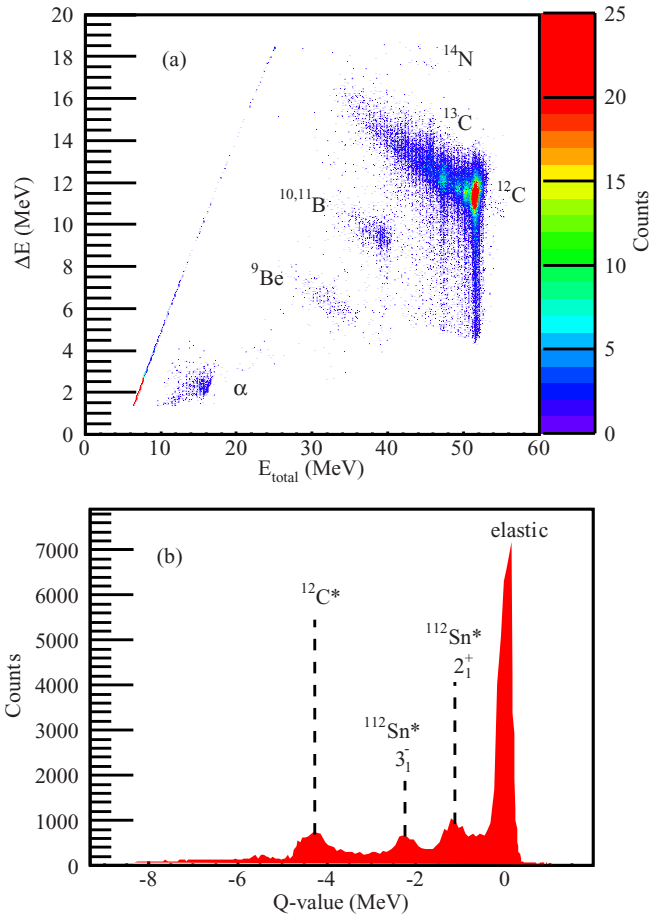

FIG. 2. (a) Typical two-dimensional (ΔE versus E_{total}) gain-matched spectrum showing the outgoing projectilelike fragments at $\theta_{\text{lab}} = 70^\circ$ in the $^{12}\text{C} + ^{112}\text{Sn}$ reaction. (b) One-dimensional spectrum showing Q-value distribution of elastic and inelastic scattering.

In addition, few states corresponding to one-neutron pickup (^{12}C, ^{13}C) as well as one-proton stripping (^{12}C, ^{11}B), with subsequent excitation of the respective residual nuclei, could be identified. All these channels are included into the theoretical modeling of the reaction system to constrain the calculations and lead to realistic potential and coupling parameters.

The yields for the elastic scattering and low-lying excited (2_1^+ and 3_1^-) states of target are extracted for determining their differential cross sections, which are then translated to the center-of-mass frame. The angular distributions for the elastic-to-Rutherford ratio are shown as hollow circles in Figs. 3(a)–3(f). The average statistical errors on the elastic scattering cross sections are typically 1−2% over the entire angular range, except for 4−5% at extreme backward angles. The experimental cross sections for the $\lambda = 2$ transition in each Sn isotope are shown as squares in Figs. 3(g)–3(l), and as triangles in Figs. 3(m)–3(r) for the $\lambda = 3$ transition. The lines in all figures represent the results of theoretical calculations described in Sec. III A and III B.

III. THEORETICAL CALCULATIONS

A. Coupled reaction channels (CRC) framework

CRC model calculations for elastic and inelastic scattering angular distributions have been performed using FRESCO by coupling the major direct reaction channels to the entrance channel, in the coupled channels Born approximation (CCBA) limit. The strongly coupled elastic and inelastic scattering channels are solved exactly and blocked together to be treated as a single unit during successive iterations for numerical convergence. The weaker transfer couplings are treated as perturbations. The coupling scheme for one of the systems is shown in Fig. 4. Since the cumulative coupling effect of all open reaction channels in a colliding system is essentially manifested into the elastic scattering cross section, the wave functions for the different model space channels are generated from a phenomenological optical potential, with real and imaginary components of Woods-Saxon (WS) volume form, whose parameters are determined by reproducing the measured elastic scattering data for each system. The total potential can be defined as:

$$V_{\text{total}}(r) = V_c(r, r_c) - \frac{V_0}{1 + \exp\left(\frac{r - r_0}{a_0}\right)} - \frac{iW_0}{1 + \exp\left(\frac{r - r_w}{a_w}\right)}. \tag{2}$$

Here, $V_c(r, r_c)$ is the Coulomb potential due to a uniformly charged sphere of radius $R_c = r_c(A_P^{1/3} + A_T^{1/3})$, with r_c fixed at 1.20 fm and A_P and A_T are the mass numbers of projectile and target, respectively. The potential (mass) radius parameter is calculated as an average of r_0 and r_w. The long-range volume imaginary potential used for the entrance channel accounts for the flux loss due to (i) compound nuclear reactions and (ii) direct reaction channels that are not included in the model space (such as higher excitations in the projectile or target, multinucleon/cluster transfers). The final potential parameters used in the CRC calculations that provide optimum description of elastic as well as nonelastic channels are listed in Table I.

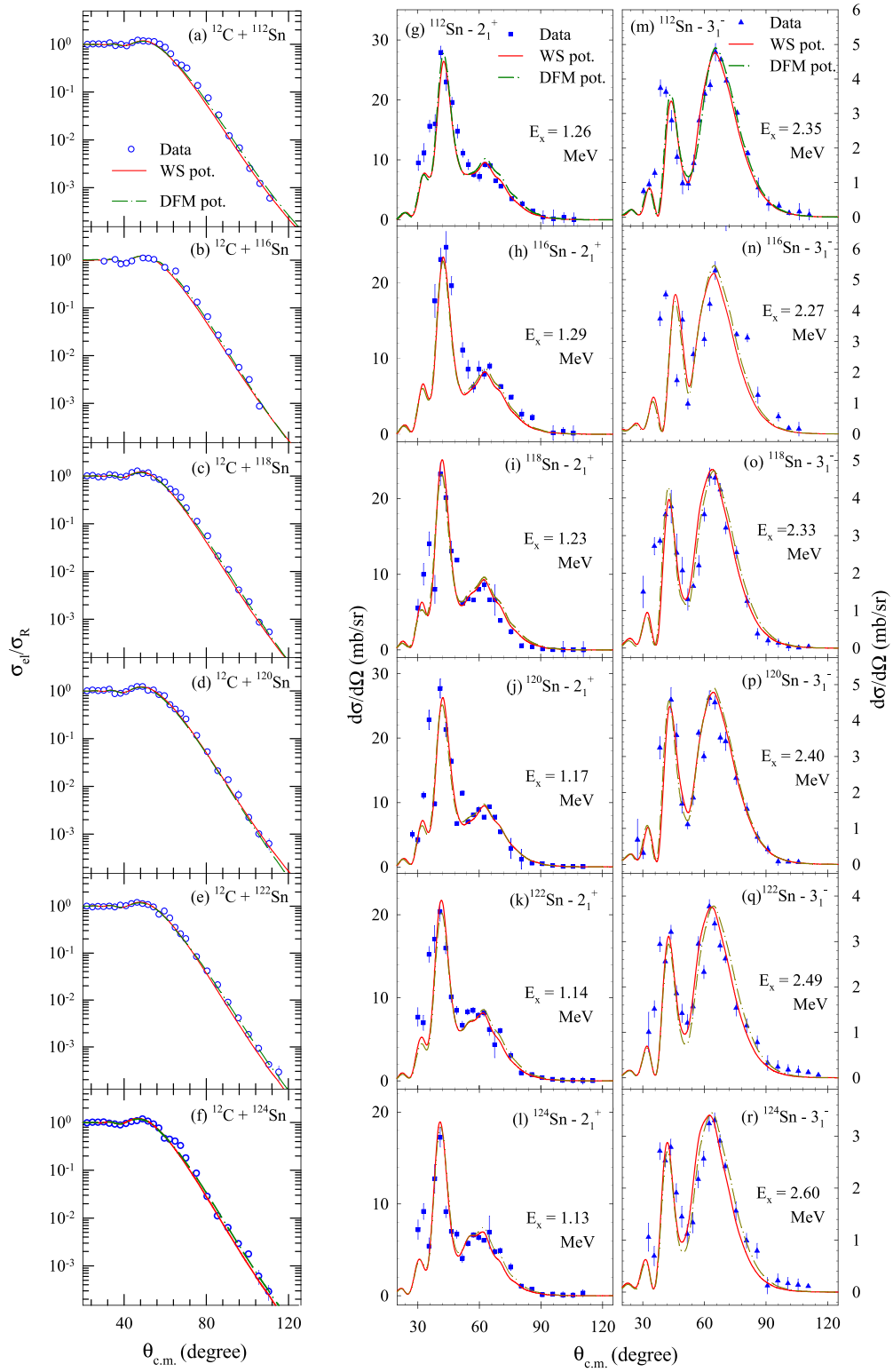

FIG. 3. Experimental angular distributions and results of CRC calculations (solid lines for WS potential, dash-dotted lines for DFM potential) for (a)–(f) elastic-to-Rutherford cross section ratio, and (g)–(l) target inelastic scattering to 2_1^+ (squares) and (m)–(r) 3_1^- (triangles up) states, in ^{12}C + ^{112,116,118,120,122,124}Sn systems at $E_{lab} = 60$ MeV.

Among the various nonelastic channels, the coupling of the first excited 2^+ state of ^{12}C is found to have considerable influence on the elastic scattering angular distribution. Several studies in the past report an oblate nature of the deformation of ^{12}C nucleus in its 2^+ state, confirmed by exclusive measurements [17,18] of the spectroscopic quadrupole moment (reorientation coupling), $Q_S(2^+)$, in the range of 0.06–0.07 eb. This translates to an intrinsic quadrupole

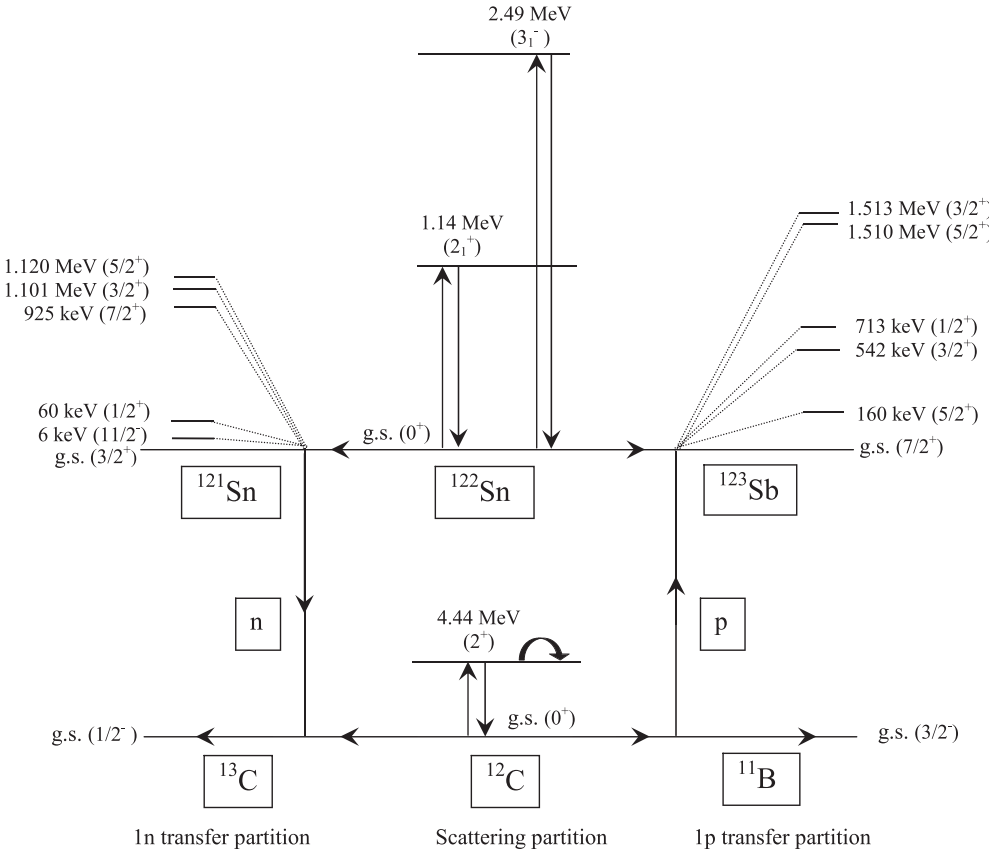

FIG. 4. Coupling scheme of the $^{12}C + ^{122}Sn$ system used for the CRC calculations in FRESCO.

moment of −0.21 eb in the body-fixed frame, which supports a substantial oblate deformation. A compilation [19] of the deformation length for this excitation in ^{12}C obtained from several existing measurements with a variety of probes shows scattered values, ranging from −1.42 fm to −1.76 fm. In the present work, the deformation lengths are suitably adjusted, and kept same for the Coulomb potential and the real and imaginary parts of the nuclear potential. The reorientation coupling is also defined, which is found to be crucial in order to reproduce the elastic data at the extreme backward angles. The extracted values, $\delta^{ch} = \delta^{m} = -1.38$ fm, $B(E2; 0^+ \rightarrow 2^+) = 29.5\,e^2fm^4$ and $Q_S(2^+) = 0.05$ eb, lead to an optimum agreement between the calculated (solid lines) and measured (symbols) cross sections as shown in Figs. 5(a) and 5(b) for the $^{12}C^*(4.44\ MeV) + ^{118,122}Sn$ systems. The calculated cross sections are found to be highly sensitive to the sign of the deformation lengths for the ^{12}C excitation. One fails to reproduce the angular positions of the maxima by considering prolate deformations, with $\delta^{ch} = \delta^{m} = 1.38$ fm, or with unequal values, $\delta^{ch} = 1.38$ fm, $\delta^{m} = 0.90$ fm (as shown with dashed and dash-dotted lines in Fig. 5). The angular distribution obtained from heavy-ion inelastic scattering is, therefore, a sensitive tool for identifying prolate or oblate nature of an excitation.

TABLE I. Entrance channel WS potential parameters used in CRC calculations for systems with different Sn targets. Values of r_0 and r_w were fixed at 1.175 fm and 1.150 fm, respectively.

Target	V_0 (MeV)	a_0 (fm)	W_0 (MeV)	a_w (fm)
^{112}Sn	49.70	0.725	23.13	0.670
^{116}Sn	52.85	0.702	26.50	0.613
^{118}Sn	63.75	0.705	38.32	0.620
^{120}Sn	56.65	0.675	37.81	0.551
^{122}Sn	50.45	0.712	39.60	0.595
^{124}Sn	58.85	0.702	40.44	0.612

The target excited states are treated as collective vibrational states. The calculations require adjustments of δ_λ^{ch} and δ_λ^{m} values (owing to CNI), to reproduce the inelastic scattering angular distributions in Figs. 3(g)–3(r). For the $\lambda = 2$ transition in each isotope, δ_2^{ch} is nearly consistent with existing Coulomb excitation measurements of $B(E2)$ [4,5,7,8], while δ_2^{m} is larger than δ_2^{ch} by about ≈5–7%. The calculations are shown by solid lines in Figs. 3(g)–3(l). For the $\lambda = 3$ transition, the calculations are found to be less sensitive to the δ_3^{ch} parameter, and the best fits for ^{112,118,120,124}Sn are obtained by using δ_3^{ch} values from an existing Coulomb excitation measurement [10] that are fairly closer to the data compared to other $B(E3)$ estimates [9,11,12,14]. The δ_3^{ch} values for ^{116,122}Sn are suitably adjusted (reduced) for a better reproduction of the experimental data, as Ref. [10] reports much larger values for these two isotopes

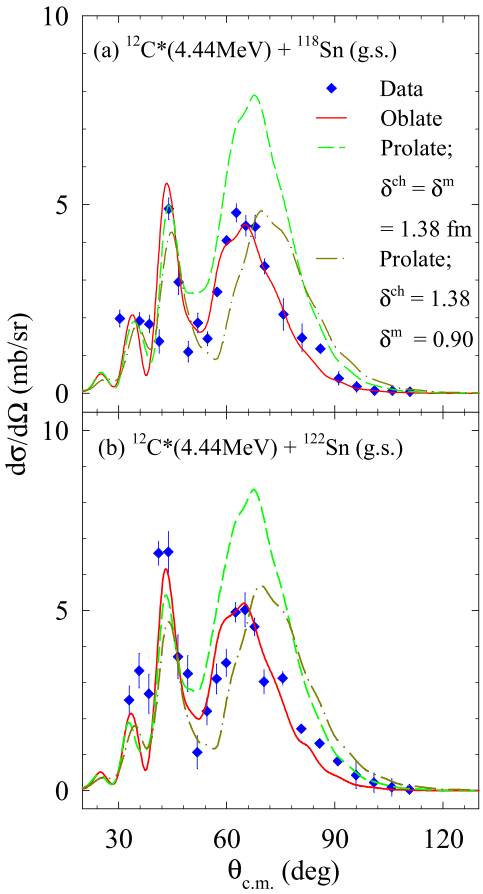

FIG. 5. Experimental differential cross sections (diamonds) for inelastic excitation of ^{12}C in (a) $^{12}\mathrm{C} + {}^{118}\mathrm{Sn}$ and (b) $^{12}\mathrm{C} + {}^{122}\mathrm{Sn}$ systems. The lines show CRC calculations for: (i) $\delta^{ch} = \delta^{m} = -1.38$ fm; $Q_S = +0.05$ eb (solid), (ii) $\delta^{ch} = \delta^{m} = +1.38$ fm (dashed), and (iii) $\delta^{ch} = +1.38$ fm and $\delta^{m} = +0.90$ fm (dash-dotted). Calculation with parameter set (i) is found to suitably agree with the data and these parameters are used for complete theoretical modeling in the present systems.

compared to their neighbors. The δ_3^m values are nearly independent of fluctuations in δ_3^{ch}, and have been determined by exclusively normalizing to the data beyond the valley region in Figs. 3(m)–3(r). The corresponding calculations are shown by solid lines. Interestingly, the δ_2^{ch} and δ_3^{ch} values of the deformed Coulomb potential are similar to the values deduced from ^{7}Li-induced excitations [16]. However, the values of δ_2^m and δ_3^m had to be varied, which establishes a characteristic probe dependence. The extracted $\delta_\lambda^{ch,m}$ values that provide optimum reproduction of the data are given in Table II.

In addition to the inelastic channels of projectile and target, few dominant one-neutron pickup and one-proton stripping channels, corresponding to low-lying states of the respective residual nuclei, are also included with available spectroscopic factors. The exit channel real potential is kept to be same as that of the entrance channel, with a short-ranged imaginary potential of WS square form, given by $W_0 = 10.00$ MeV, $r_w = 1.00$ fm and $a_w = 0.40$ fm. Integrating the radial wave functions up to 20 fm in steps of 0.10 fm and summing over

TABLE II. Experimental deformation lengths for the low-lying $\lambda = 2, 3$ excitations in Sn isotopes.

Nucleus	$\lambda = 2$		$\lambda = 3$	
	[c] δ_2^{ch} (fm)	[c] δ_2^{m} (fm)	[a] δ_3^{ch} (fm)	[c] δ_3^{m} (fm)
^{112}Sn	0.709(39)	0.760(45)	0.742(109)	0.707(46)
^{116}Sn	0.651(33)	0.687(42)	[b] 0.763(083)	0.720(62)
^{118}Sn	0.649(25)	0.715(37)	0.757(092)	0.692(51)
^{120}Sn	0.665(39)	0.697(47)	0.720(115)	0.665(41)
^{122}Sn	0.615(28)	0.655(36)	[b] 0.677(076)	0.621(49)
^{124}Sn	0.572(36)	0.614(41)	0.655(107)	0.610(43)

[a]Coulomb excitation measurement [10].
[b]Modified.
[c]Present measurement.

100 partial waves is found to be adequate to attain numerical convergence.

The chosen parameter set for the optical potential governing these interactions, given in Table I, is not unique. There are various such sets which reproduce the data equally well. However, once a consistent description of elastic and inelastic scattering channels is attained, it is observed that the combination of real and imaginary radii required to explain the data always led to δ_λ^m similar to those reported in Table II.

B. Sensitivity of interaction potential

The optical model potential used above for interpretation of elastic and inelastic scattering is largely phenomenological. It does not incorporate the microscopic aspects of the reaction and excitation mechanism, where one seeks to describe the scattering of the projectile from a nucleus in terms of fundamental interactions between the nucleons. In order to compare the results with those using a microscopic potential, the CRC calculations are repeated with a density-dependent double folding model (DFM) nucleus-nucleus potential calculated as a function of center to center separation, r, as

$$V_{\mathrm{DFM}}(\mathbf{r}) = \int d\mathbf{r}_1 \int d\mathbf{r}_2 \left[v_{00}(\mathbf{r} + \mathbf{r}_2 - \mathbf{r}_1).\left(\rho_{g.s.}^{1n} + \rho_{g.s.}^{1p}\right) \times \left(\rho_{g.s.}^{2n} + \rho_{g.s.}^{2p}\right)\right]. \quad (3)$$

Here, v_{00} is the fundamental nucleon-nucleon interaction parametrized in the M3Y Paris form [20], and folded over the particle densities. Since ^{12}C is an isoscalar probe ($N = Z = 6$), the interaction has no isospin-dependent component. The shapes of the proton and neutron ground-state densities $\rho_{g.s.}^{(p,n)}$ of the projectile (1) and target (2) are taken to be analogous to their ground-state charge density distributions obtained from existing electron scattering measurements [21,22]. The r.m.s. radii for the point-proton distributions in projectile and target are deduced from the radii of their measured charge distributions, by unfolding the charge distribution of the proton as well as a minor, but important, contribution from the charge distribution of neutron (with a nonvanishing mean square charge radius) [23]. For the ^{12}C nucleus, the neutron and proton distributions are considered to be equal [24]. For the Sn nuclei, the radii for the neutron density distributions are

TABLE III. Normalization coefficients, N_r and N_i, for the real and imaginary parts of the DFM potential for the interaction between ^{12}C and different Sn isotopes.

Target	N_r	N_i
^{112}Sn	1.00	0.33
^{116}Sn	1.00	0.28
^{118}Sn	1.00	0.35
^{120}Sn	1.00	0.28
^{122}Sn	1.00	0.40
^{124}Sn	1.00	0.35

kept consistent with their measured skin thicknesses [25,26]. A complex form of the bare DFM potential is used in the full CRC calculations to generate optimum description of elastic scattering, with adjustable normalization coefficient for the imaginary part, N_i, as given in Table III.

For the inelastic excitations of the Sn isotopes, the DFM calculations have been carried out with the same $\delta_\lambda^{ch,m}$ values as reported in Table II. Interestingly, the calculations for elastic scattering and target excitations are found to give adequate representation of the data and are in good agreement with the results of the WS potential. The results are shown by dash-dotted lines for the 2_1^+ state in Figs. 3(g)–3(l) as well as for the 3_1^- state in Figs. 3(m)–3(r). This implies that the extracted deformation lengths are independent of the choice of interaction potential and method of scattering analysis, provided that a consistent description of both elastic and inelastic scattering is obtained.

IV. TRANSITION MATRIX ELEMENTS

Additional information about the structure of the 2_1^+ and 3_1^- states can be extracted by studying the ratio of the multipole neutron and proton transition matrix elements, M_n/M_p. This ratio depends on the relative contribution of the neutron and proton configurations. From the experimental information of δ_λ^m and δ_λ^{ch}, as reported in Table II, the microscopic neutron and proton deformation lengths, $\delta_\lambda^{(n,p)}$, can be disentangled as described in Refs. [1,27]. Empirically, it is assumed that $\delta_\lambda^p \approx \delta_\lambda^{ch}$ and $\delta_\lambda^m \approx \frac{Zb_p\delta_\lambda^p + Nb_n\delta_\lambda^n}{Zb_p+Nb_n}$, where $b_{n(p)}$ are microscopic bare interactions of the external field/probe with the neutrons (protons) of the target. For the ^{12}C probe, the ratio of the neutron and proton field strengths is taken to be unity. The deduced $\delta_\lambda^{(n,p)}$ values are summarized in Table IV. The corresponding neutron and proton multipole transition matrix elements are commonly written as [28],

$$M_{(n,p)} = \int_0^\infty r^{\lambda+2}\rho_{tr,\lambda}^{(n,p)}dr, \tag{4}$$

where the phenomenological transition densities are derived using Bohr-Mottelson prescription [29], given by $\rho_{tr,\lambda}^{(n,p)} = -\delta_\lambda^{(n,p)}\frac{d\rho_{g.s.}^{(n,p)}}{dr}$. This leads to the collective model ratio, $M_n/M_p = \frac{N\langle r^{\lambda-1}\rangle_n\delta_\lambda^n}{Z\langle r^{\lambda-1}\rangle_p\delta_\lambda^p}$, which acts as a tool for identifying the relative participation of neutrons and protons in a transition. Here, the underlying assumption is that proton and neutron densities are proportional to each other with Z and N factors, and the radial moments $\langle r^{\lambda-1}\rangle_{n,p}$ are taken over the g.s. densities. For homogeneous vibrations, neutron and proton densities are expected to have the same radial shape and one would obtain $\delta_\lambda^n = \delta_\lambda^p$. Any deviation may imply inhomogeneity in a transition.

Using the results of $\delta_\lambda^{(n,p)}$ in the equations given above, the values of M_n/M_p ratios corresponding to $\lambda = 2$ and 3 have been determined for the different Sn isotopes. The results are summarized in Table IV as well as in Fig. 6. Both the $\lambda = 2$ (triangles up) and $\lambda = 3$ (triangles down) transitions closely follow the N/Z trend represented by the solid line. Within errors, both transitions can be considered to be in good agreement with collective model prescription when probed using the isoscalar ^{12}C nucleus. Recent results obtained using a complementary probe,^{7}Li [16], show a significant deviation from N/Z for $\lambda = 3$ transition (hollow circles) in all Sn isotopes. This hints at a possible inhomogeneity for the octupole excitation in Sn when probed using ^{7}Li, which is not seen with the ^{12}C probe. For the $\lambda = 2$ transition, the neutron collectivity observed in the present study with the ^{12}C projectile is nearly similar to that observed earlier with the ^{7}Li projectile [16]. The two sets of measurements predict different M_n/M_p ratios. As the electromagnetic interaction is model independent, it can be concluded that measurements of mass deformation lengths are largely probe dependent,

TABLE IV. Experimental values of microscopic proton and neutron transition parameters corresponding to $\lambda = 2, 3$ excitations in Sn isotopes obtained from present measurements.

Nucleus	N/Z	$\lambda = 2$					$\lambda = 3$				
		$\delta_2^{ch} = \delta_2^p$ (fm)	δ_2^n (fm)	M_n/M_p	$B(E2)$ (e^2b^2)	$B(IS2)$ (e^2b^2)	[a]$\delta_3^{ch} = \delta_3^p$ (fm)	δ_3^n (fm)	M_n/M_p	[a]$B(E3)$ (e^2b^3)	$B(IS3)$ (e^2b^3)
^{112}Sn	1.24	0.709(39)	0.804(69)	1.41(18)	0.242(23)	0.251(25)	0.742(109)	0.684(093)	1.19(17)	0.087(12)	0.081(17)
^{116}Sn	1.32	0.651(33)	0.693(72)	1.45(19)	0.207(20)	0.211(28)	[b] 0.763(083)	0.662(101)	1.21(21)	[b]0.098(13)	0.090(19)
^{118}Sn	1.36	0.649(25)	0.744(65)	1.58(16)	0.208(16)	0.246(31)	0.757(092)	0.617(095)	1.16(24)	0.097(17)	0.087(19)
^{120}Sn	1.40	0.665(39)	0.718(63)	1.56(22)	0.217(21)	0.242(38)	0.720(115)	0.625(094)	1.29(28)	0.090(14)	0.082(16)
^{122}Sn	1.44	0.615(28)	0.682(67)	1.63(18)	0.191(17)	0.216(30)	[b] 0.677(076)	0.584(085)	1.33(23)	[b]0.082(14)	0.074(18)
^{124}Sn	1.48	0.572(36)	0.621(71)	1.67(22)	0.167(21)	0.185(29)	0.655(107)	0.541(102)	1.31(32)	0.073(11)	0.067(14)

[a]Coulomb excitation measurement [10].
[b]Modified.

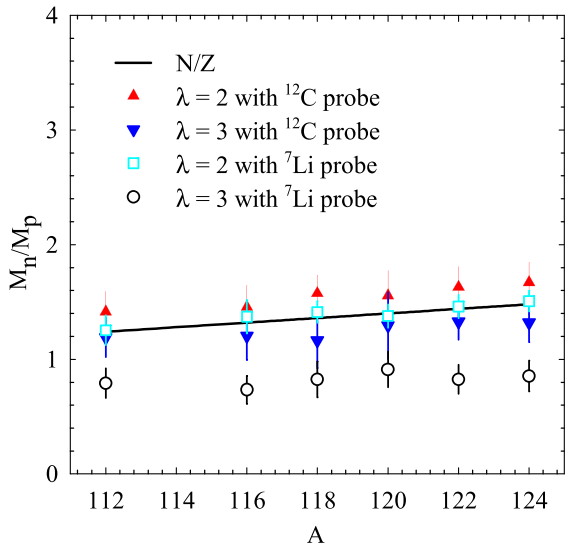

FIG. 6. The M_n/M_p ratios for low-lying $\lambda = 2$ (triangles up) and $\lambda = 3$ (triangles down) excitations in Sn isotopes probed by ^{12}C nucleus. The hollow squares and circles represent the corresponding results with the ^{7}Li projectile [16]. The solid line shows the homogeneous value of N/Z.

relying heavily on the interaction potential with the incoming projectile, convoluted over its finite size.

For strongly absorbed heavy-ion probes, the scattering cross section in the regions of the Coulomb and nuclear fields is proportional to the respective matrix elements. The electromagnetic transition probability is directly related to the charge deformation, and in turn, the proton transition matrix element as $B(E\lambda) = |M_p|^2$. An analogous quantity related to the mass deformation of the nucleus is often defined, in which neutrons and protons maintain their equilibrium density ratios, known as the isoscalar transition probability [30]

$$B(IS\lambda) = \left(\frac{Z}{A}\right)^2 |M_n + M_p|^2. \tag{5}$$

With the present results of M_n/M_p, the $B(E\lambda)$ and $B(IS\lambda)$ values have been determined and are reported in Table IV. The errors on all the above quantities are assigned by propagating the errors on the corresponding δ_λ^{ch} and δ_λ^{m} values extracted from the model calculations. One observes (see Table IV) that the isoscalar ^{12}C probe excites predominantly homogeneous mass vibrations for the $\lambda = 2, 3$ transitions, with nearly similar $B(E\lambda)$ and $B(IS\lambda)$ values.

V. INTRINSIC DEFORMATION LENGTHS

For nuclear inelastic scattering from statically deformed nuclei, Hendrie [31] suggested a simple procedure for removing the effects of finite projectile radius in the extraction of nuclear potential shapes. The prescription can also be extended to nuclei with vibrational modes of excitations. Here, the underlying assumption is that the probes and the targets interact only at their mutual sharply defined surfaces. With the center of mass at the origin of the body-fixed frame and an axially symmetric shape, the edge of a spherical nucleus of radius R_0 deformed by quadrupole and octupole vibrations can be written as:

$$\begin{aligned} R(\theta) &= R_0[1 + \beta_{20}Y_{20}^*(\theta) + \beta_{30}Y_{30}^*(\theta)] \\ &= R_0[1 + \varepsilon(\theta)] \end{aligned} \tag{6}$$

with β_{20}, β_{30} being the intrinsic deformation parameters, and Y_{20}, Y_{30} being the spherical harmonics characterizing the shape of the nucleus. The transition amplitudes of a nucleus are found to depend sensitively on the chosen radius, which is largely probe dependent. When a projectile of size (radius) Δ probes the dynamically deformed target surface, the locus of the center of the projectile describes a surface with radius [19,31],

$$r(\theta) = r_0 + \delta_2(\Delta)Y_{20}^*(\theta) + \delta_3(\Delta)Y_{30}^*(\theta). \tag{7}$$

Here, r_0 characterizes the spatial extension of the optical potential, and defines the potential radius for the target nucleus in its ground state. The quantities $\delta_\lambda(\Delta)$ are the experimentally determined deformation lengths for target excitation of multipolarity λ. These are constrained by the choice of the probe and the corresponding interaction radius parameter, and can be written as [31]:

$$\delta_\lambda(\Delta) = \delta_\lambda(0) + \frac{1}{2}\frac{R_0\Delta}{R_0 + \Delta}\int Y_{\lambda 0}\varepsilon'(\theta)^2 d\Omega, \tag{8}$$

where $\delta_\lambda(0) \equiv \beta_{\lambda 0}R_0$ defines the intrinsic nuclear deformation length. The quantities Δ and R_0 are considered to be measures of the point-matter radii for the probes and the targets, respectively. The r.m.s. radii for the point-matter distributions for all nuclei are deduced from their measured charge r.m.s. radii, by unfolding the charge distributions of the proton and the neutron, with $\langle r_m^2\rangle = \langle r_{ch}^2\rangle - 0.722 + (\frac{N}{Z})0.115$ fm^2. Here, the mean square charge radius of the proton is 0.722 fm^2 (consistent with electron scattering [21] and muonic hydrogen Lamb-shift measurements [32]) and mean square charge radius of the neutron is -0.115 fm^2 (from measurements of neutron-electron scattering length [23]).

For the vibrational Sn nuclei, the 2_1^+ and 3_1^- states have been studied with a variety of projectiles for which the deformation lengths can be written as functions of the probe size Δ,

$$\delta_2(\Delta) = \delta_2(0) + \frac{R_0\Delta}{R_0 + \Delta}\left(0.270\beta_{20}^2 + 0.756\beta_{30}^2\right) \tag{9}$$

$$\delta_3(\Delta) = \delta_3(0) + \frac{R_0\Delta}{R_0 + \Delta}(0.505\beta_{20}\beta_{30}). \tag{10}$$

Combining the results for $\delta_\lambda(\Delta)$ of the present work using ^{12}C probe with the ones from the existing measurements using other probes such as p [14], d [33], ^{3}He [34], α [9], ^{6}Li [35], ^{7}Li [16], and ^{10}B [36], a systematic analysis has been made over a range of Δ values. Using Eqs. (9) and (10), the parameters $\delta_2(0)$ and $\delta_3(0)$ from the best-fit curves to the experimental values of $\delta_2(\Delta)$ and $\delta_3(\Delta)$, respectively, provide probe-independent intrinsic $\lambda = 2$ and $\lambda = 3$ matter deformation lengths for the Sn isotopes. The results are summarized in Table V and in Fig. 7. With same radial shape for the intrinsic neutron and proton density deformations, one can write the

TABLE V. Intrinsic matter deformation lengths and corresponding M_n/M_p ratios for the Sn isotopes.

Nucleus	$\lambda = 2$		$\lambda = 3$	
	$\delta_2(0)$ (fm)	M_n/M_p	$\delta_3(0)$ (fm)	M_n/M_p
^{112}Sn	0.840(102)	1.67(24)	0.945(201)	1.84(38)
^{116}Sn	0.743(068)	1.69(17)	0.952(172)	1.88(31)
^{118}Sn	0.731(083)	1.67(20)	0.917(148)	1.85(29)
^{120}Sn	0.718(096)	1.62(22)	0.844(121)	1.82(25)
^{122}Sn	0.677(059)	1.68(14)	0.810(122)	1.91(28)
^{124}Sn	0.644(078)	1.76(18)	0.777(134)	1.92(30)

ratio of their corresponding transition matrix elements as:

$$\frac{M_n}{M_p} = \frac{\delta_\lambda(0)}{\delta_\lambda^{ch}}\left(1 + \frac{N}{Z}\right) - 1 \qquad (11)$$

with δ_λ^{ch} taken from Table II. The results are shown in Table V and also in Fig. 8 as circles and squares for the $\lambda = 2$ and $\lambda = 3$ transitions, respectively. It may be interesting to note that the M_n/M_p ratios obtained here are larger compared to those in Fig. 6. Particularly for the $\lambda = 3$ transition, the M_n/M_p ratios now lie above the N/Z values, in contrast to the ones in Fig. 6. This approach shows that neutron collectivity is the dominant contribution to both the 2_1^+ and 3_1^- target excitations, as may be expected in proton-magic Sn isotopes. Clearly, the ratio of the neutron and proton transition densities (M_n/M_p) do not simply scale as N/Z as often assumed in the collective model. The present results for the $\lambda = 2$ transition are found to be in good agreement with those obtained from a systematic study of M_n/M_p for single-closed-shell nuclei reported in Ref. [1]. The uncertainties in the intrinsic deformation lengths and M_n/M_p ratios that may arise due to discrepancies among various measurements of r.m.s. nuclear charge radii are estimated to be very small.

The results have been compared with microscopic calculations employing quasiparticle random phase approximation (QRPA) [38] within the quasiparticle-phonon model [39] (dashed and dash-dot-dotted lines in Fig. 8) that accounts for the fact that the proton system in Sn is closed (magic) and collectivity is largely caused by neutrons. The QRPA approach leads to larger ratios for the $\lambda = 2$ transition as neutron number increases, while the trend is in decent agreement with the extracted intrinsic ratio for the $\lambda = 3$ transition.

A. Dependence on nature of probe-target interaction

In addition to the probe size, the nature of interaction between the probe and the target is another factor that is expected to contribute towards the discrepant transition rates observed in Sn isotopes across a range of probes. The cumulative effect is contained in the δ_λ^m values extracted in each measurement with a different projectile. Once the effect of the projectile size is eliminated, and proton and neutron distributions are considered to have same radial shape, the ratio $\frac{\delta_\lambda^m}{\delta_\lambda^{ch}} \approx \frac{1+\frac{b_n}{b_p}\frac{M_n}{M_p}}{1+\frac{b_n}{b_p}\frac{N}{Z}}$ is expected to accentuate the effect of solely the nature of

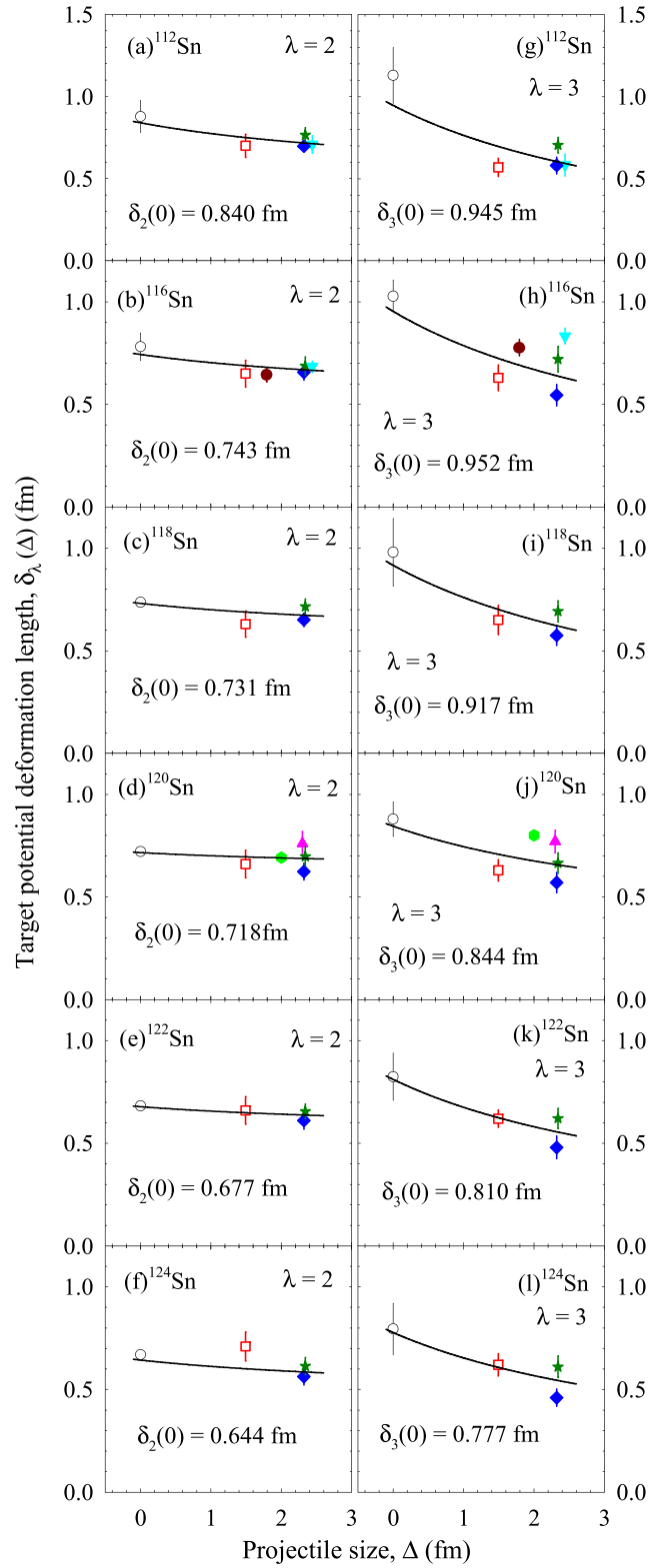

FIG. 7. Nuclear inelastic scattering deformation lengths for the (a)–(f) $\lambda = 2$ and (g)–(l) $\lambda = 3$ excitations in Sn isotopes as a function of probe size Δ. The measurements are with a variety of probes such as p (hollow circles) [14,37], d (hexagons) [33], ^{3}He (filled circles) [34], α (squares) [9], ^{6}Li (filled triangles down) [35], ^{7}Li (diamonds) [16], ^{10}B (filled triangles up) [36], and ^{12}C (stars; present work). The curves are best fits to Eqs. (9) and (10).

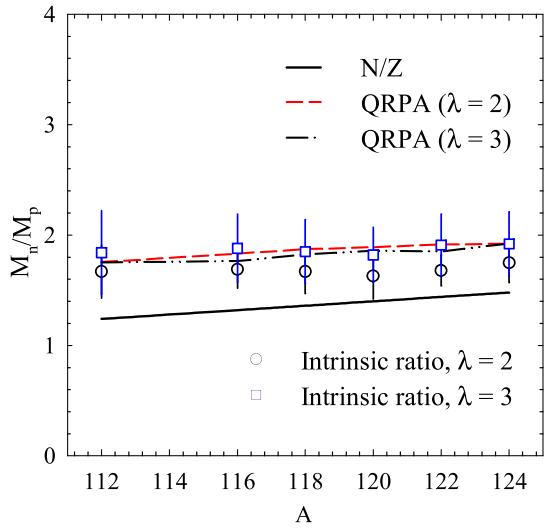

FIG. 8. Intrinsic M_n/M_p ratios for low-lying excitations in Sn isotopes corresponding to $\lambda = 2$ (circles) and $\lambda = 3$ (squares) transitions. The solid line shows the homogeneous trend of N/Z. The dashed and dash-dot-dotted lines represent the results of QRPA calculations for 2_1^+ and 3_1^- transitions, respectively [38].

interaction between the probe and the target, surmised by the corresponding b_n/b_p ratio, as introduced earlier in Sec. IV. For the proton-induced reactions, Ref. [1] puts $b_n/b_p = 3$, while for the isoscalar projectiles such as α, ^{12}C, one obtains $b_n/b_p = 1$. Using the veritable M_n/M_p values for the Sn isotopes as reported in Table V, one obtains a difference of a mere $\approx$5% between the $\frac{\delta_2^m}{\delta_2^{ch}}$ ratios, and a corresponding difference of $\approx$10% between the $\frac{\delta_3^m}{\delta_3^{ch}}$ ratios, from the proton and heavy-ion induced excitations. Thus, for the projectiles considered in the present study, the crucial factor for the extraction of intrinsic deformation lengths of the Sn isotopes is the removal of finite probe size. Thereafter, one observes that the effect of the nature of probe-target interaction is rendered insignificant.

VI. SUMMARY

A systematic study of the characteristics of the 2_1^+ and 3_1^- excited states in ^{112,116,118,120,122,124}Sn is presented, by means of heavy-ion inelastic scattering using isoscalar ^{12}C beam as probe at $E_{\rm lab} = 60$ MeV. The deformation lengths and transition probabilities are extracted via extensive CRC calculations employing the collective model approach. Under the phenomenological approximation that neutron and proton transition densities scale as N/Z in collective excitations, reasonable agreement is seen between their respective deformation lengths for all the Sn isotopes, with the ratio of neutron and proton transition matrix elements $M_n/M_p \sim N/Z$ for both the $\lambda = 2$ and $\lambda = 3$ transitions. The results are compared with those obtained via scattering of another heavy-ion projectile, ^{7}Li, at similar $E_{\rm c.m.}/V_{\rm B}$. It is observed that such measurements are highly dependent on the choice of probe as well as the interaction radius parameter. A prescription to remove the effects of projectile size is used to deduce the intrinsic mass deformation length for each isotope. The results indicate that neutron collectivity is the dominant contribution to the 2_1^+ and 3_1^- excited states in the Sn isotopes, as may be expected in proton-magic nuclei. The effect of size of the probe is the dominant factor that leads to discrepant transition rates; the nature of probe-target interaction is secondary. Extensive measurements using a variety of probes is essential for understanding the basic collective phenomena in low-lying transitions along an isotopic chain of stable neutron-excess nuclei. The present considerations illustrate the path and problems that would arise when one discusses the deformation properties of the proton and neutron distributions along a stable/unstable isotopic chain of similar complexity.

ACKNOWLEDGMENTS

The financial support of BRNS through the Project No. 2012/21/11-BRNS/1090 is greatly acknowledged. We are also grateful to the Pelletron crew for smooth operation of the accelerator during the experiment.

[1] A. M. Bernstein, V. R. Brown, and V. A. Madsen, Comments Nucl. Part. Phys. **11**, 203 (1983).
[2] I. J. Thompson and F. M. Nunes, *Nuclear Reactions for Astrophysics* (Cambridge University Press, New York, 2009).
[3] N. Austern and J. S. Blair, Ann. Phys. (NY) **33**, 15 (1965).
[4] P. H. Stelson, F. K. McGowan, R. L. Robinson, and W. T. Milner, Phys. Rev. C **2**, 2015 (1970).
[5] R. Graetzer, S. M. Cohick, and J. X. Saladin, Phys. Rev. C **12**, 1462 (1975).
[6] J. Bryssinck, L. Govor, V. Y. Ponomarev, F. Bauwens, O. Beck, D. Belic, P. vonBrentano, D. DeFrenne, T. Eckert, C. Fransen, K. Govaert, R. D. Herzberg, E. Jacobs, U. Kneissl, H. Maser, A. Nord, N. Pietralla, H. H. Pitz, and V. Werner, Phys. Rev. C **61**, 024309 (2000).
[7] J. M. Allmond, A. E. Stuchbery, A. Galindo-Uribarri, E. Padilla-Rodal, D. C. Radford, J. C. Batchelder, C. R. Bingham, M. E. Howard, J. F. Liang, B. Manning *et al.*, Phys. Rev. C **92**, 041303(R) (2015).
[8] R. Kumar, M. Saxena, P. Doornenbal, A. Jhingan, A. Banerjee, R. K. Bhowmik, S. Dutt, R. Garg, C. Joshi, V. Mishra *et al.*, Phys. Rev. C **96**, 054318 (2017).
[9] G. Bruge, J. C. Faivre, H. Faraggi, and A. Bussiere, Nucl. Phys. A **146**, 597 (1970).
[10] N. G. Jonsson, A. Backlin, J. Kantele, R. Julin, M. Luontarna, and A. Passoja, Nucl. Phys. A **371**, 333 (1981).
[11] R. H. Spear, A. M. Baxter, S. M. Burnett, and C. L. Miller, Aust. J. Phys. **42**, 41 (1989).
[12] T. H. Curtis, R. A. Eisenstein, D. W. Madsen, and C. K. Bockelman, Phys. Rev. **184**, 1162 (1969).
[13] P. Barreau and J. B. Bellicard, Phys. Rev. Lett. **19**, 1444 (1967).
[14] O. Beer, A. E. Behay, P. Lopato, Y. Terrien, G. Vallois, and K. K. Seth, Nucl. Phys. A **147**, 326 (1970).

[15] N. Baron, R. F. Leonard, J. L. Need, W. M. Stewart, and V. A. Madsen, Phys. Rev. **146**, 861 (1966).
[16] A. Kundu, S. Santra, A. Pal, D. Chattopadhyay, R. Tripathi, B. J. Roy, T. N. Nag, B. K. Nayak, A. Saxena, and S. Kailas, Phys. Rev. C **99**, 034609 (2019).
[17] W. Vermeer, M. Esat, J. Kuehner, R. Spear, A. Baxter, and S. Hinds, Phys. Lett. B **122**, 23 (1983).
[18] M. K. Raju, J. Orce, P. Navrátil, G. Ball, T. Drake, S. Triambak, G. Hackman, C. Pearson, K. Abrahams, E. Akakpo *et al.*, Phys. Lett. B **777**, 250 (2018).
[19] W. Thompson and J. Eck, Phys. Lett. B **67**, 151 (1977).
[20] G. R. Satchler and W. G. Love, Phys. Rep. **55**, 183 (1979).
[21] C. W. De Jager, H. De Vries, and C. De Vries, Atomic Data and Nuclear Data Tables **14**, 479 (1974).
[22] I. Angeli and K. Marinova, Atomic Data and Nuclear Data Tables **99**, 69 (2013).
[23] S. Kopecky, J. A. Harvey, N. W. Hill, M. Krenn, M. Pernicka, P. Riehs, and S. Steiner, Phys. Rev. C **56**, 2229 (1997).
[24] H. Rebel, *Elastic and Inelastic Scattering of Alpha Particles and the Folding Model*, Lectures presented at the International School of Nuclear Physics (Predeal, Romania, 1974).
[25] S. Terashima, H. Sakaguchi, H. Takeda, T. Ishikawa, M. Itoh, T. Kawabata, T. Murakami, M. Uchida, Y. Yasuda, M. Yosoi *et al.*, Phys. Rev. C **77**, 024317 (2008).
[26] A. Krasznahorkay, A. Balanda, J. A. Bordewijk, S. Brandenburg, M. N. Harakeh, N. Kalantar-Nayestanaki, B. M. Nyakó, J. Timár, and A. van der Woude, Nucl. Phys. A **567**, 521 (1994).
[27] A. M. Bernstein, V. R. Brown, and V. A. Madsen, Phys. Lett. B **106**, 259 (1981).
[28] D. T. Khoa, Phys. Rev. C **68**, 011601(R) (2003).
[29] A. Bohr and B. R. Mottelson, *Nuclear Structure* (Benjamin, New York, 1975), Vol. 2.
[30] A. M. Bernstein, in *Advances in Nuclear Physics*, edited by M. Baranger and E. Vogt (Springer, Berlin, 1969), Vol. 3.
[31] D. L. Hendrie, Phys. Rev. Lett. **31**, 478 (1973).
[32] R. Pohl, A. Antognini, F. Nez, F. D. Amaro, F. Biraben, J. M. R. Cardoso, D. S. Covita, A. Dax, S. Dhawan, L. M. P. Fernandes *et al.*, Nature (London) **466**, 213 (2010).
[33] R. K. Jolly, Phys. Rev. **139**, B318 (1965).
[34] P. P. Singh, Q. Li, P. Schwandt, W. W. Jacobs, M. Saber, E. J. Stephenson, A. Saxena, and S. Kailas, Pramana - J. Phys. **27**, 747 (1986).
[35] X. Chen, Y. W. Lui, H. L. Clark, Y. Tokimoto, and D. H. Youngblood, Phys. Rev. C **76**, 054606 (2007).
[36] L. R. Gasques, A. S. Freitas, L. C. Chamon, J. R. B. Oliveira, N. H. Medina, V. Scarduelli, E. S. Rossi, M. A. G. Alvarez, V. A. B. Zagatto, J. Lubian *et al.*, Phys. Rev. C **97**, 034629 (2018).
[37] W. Makofske, W. Savin, H. Ogata, and T. H. Kruse, Phys. Rev. **174**, 1429 (1968).
[38] V. Yu. Ponomarev (private communication).
[39] V. G. Soloviev, *Theory of Atomic Nuclei: Quasiparticles and Phonons* (Institute of Physics Publishing, Bristol, 1992).